Acta Crystallographica Section D
Biological Crystallography
ISSN 0907-4449

Differential specific radiation damage in the Cu^{II}-bound and Pd^{II}-bound forms of an α-helical foldamer: a case study of crystallographic phasing by RIP and SAD

Klaus Fütterer,[a]* Raimond B. G. Ravelli,[b] Scott A. White,[a] Andrew J. Nicoll[c]‡ and Rudolf K. Allemann[c]

[a]School of Biosciences, University of Birmingham, Edgbaston, Birmingham B15 2TT, England, [b]EMBL, 6 Rue Jules Horowitz, BP 181, 38042 Grenoble CEDEX 9, France, and [c]School of Chemistry, Cardiff University, Main Building, Park Place, Cardiff CF10 3AT, Wales

‡ Present address: MRC Prion Unit, Department of Neurodegenerative Disease, Institute of Neurology, Queen Square, London WC1N 3BG, England.

Correspondence e-mail: k.futterer@bham.ac.uk

Received 24 September 2007
Accepted 6 December 2007

The high photon flux at third-generation synchrotron sources can inflict significant primary radiation damage upon macromolecular crystals, even when the crystals are cryocooled. However, specific radiation-induced structural changes can be exploited for *de novo* phasing by an approach known as radiation damage-induced phasing (RIP). Here, RIP and single-wavelength anomalous dispersion (SAD) phasing were alternatively used to derive experimental phases to 1.2 Å resolution for crystals of an α-helical 18-residue peptide, MINTS, which was derived from the neurotoxin apamin and the palladium-bound structure of which is now reported. Helix formation is induced by the binding of palladium (or copper) to two histidines spaced four residues apart, while two disulfide bonds tether the N-terminal helix to the C-terminal loop-like part of the peptide. Either RIP or SAD phasing of the palladium-bound and copper-bound forms of MINTS, which crystallized in different space groups, resulted in density maps of superb quality. Surprisingly, RIP phasing of the metal-bound complex structures of MINTS was a consequence of differential radiation damage, resting primarily on the reduction of the disulfide bonds in Pd-MINTS and on depletion of the metal sites in Cu-MINTS. Its miniprotein-like characteristics, versatile metal-binding properties and ease of crystallization suggest MINTS to be a convenient test specimen for methods development in crystallographic phasing based on either synchrotron or in-house X-ray diffraction data.

1. Introduction

The design of miniproteins with defined chemical, catalytic or interactive properties is a major challenge. Such proteins have attractive applications both as functional tools and as model systems to answer fundamental questions in chemical and structural biology (Johnsson *et al.*, 1993; Nicoll & Allemann, 2004*a*; Goodman *et al.*, 2007). For example, a series of miniature proteins was used to derive a thermodynamic scale of the helical propensity of the 20 standard amino acids which is now widely exploited in structural biology (O'Neil & DeGrado, 1990). Grafting of functional residues onto scaffolds such as pancreatic polypeptides has allowed the production of active miniature enzymes (Abrahams, 1997; Taylor *et al.*, 2001, 2002; Weston *et al.*, 2004; Nicoll & Allemann, 2004*b*) and miniature DNA-binding proteins (Turner *et al.*, 2004; Guerrero, Smart, Weston *et al.*, 2005; Guerrero, Smart, Woolley *et al.*, 2005). Recent advances have allowed us to control biological function by alterations of the redox conditions (Turner *et al.*, 2004; Weston *et al.*, 2004) or by illumination (Guerrero, Smart, Weston *et al.*, 2005; Guerrero, Smart, Woolley *et al.*,

2005), whilst enhancing properties such as thermal stability or DNA-binding specificity.

We recently described the synthesis and characterization of an 18-residue disulfide-stabilized peptide termed MINTS (Fig. 1; Nicoll *et al.*, 2006). The design of MINTS was inspired by the neurotoxic peptide apamin, the conformation of which is stabilized by two disulfide bonds and includes a C-terminal two-turn α-helix. Inverting the apamin sequence and introducing additional amino-acid substitutions resulted in a peptide (termed NTH-18) that forms an N-terminal helix stabilized by crossed disulfide bonds (Cys-4–Cys-16, Cys-8–Cys-18; Fig. 1; Nicoll *et al.*, 2005). In order to facilitate transition-metal binding, NTH-18 was mutated at positions 3 and 7, replacing a glutamine and a lysine with histidine residues. As a result, binding of Cu^{2+} ions to the histidine side chains (K_d = 5 n*M* at pH 8) induces an α-helical conformation over the ten amino-terminal amino acids and a corresponding signal can be observed by circular-dichroism (CD) spectroscopy (Nicoll *et al.*, 2006). Despite its close sequence relationship to NTH-18 and the presence of the disulfide bonds (Fig. 1), ligand-free MINTS shows no indication of helix formation in CD spectra (Nicoll *et al.*, 2006), contrary to the behaviour of NTH-18 (Nicoll *et al.*, 2005). In our previous report, MINTS in the Cu^{II}-bound form was characterized by X-ray crystallography to a resolution of 1.05 Å. In addition to Cu-MINTS, crystallization trials also included Ni^{II}-, Zn^{II}- and Pd^{II}-bound complexes of MINTS, elements that were observed to promote different levels of α-helical content in CD experiments . While the Ni^{II}-bound and Zn^{II}-bound complexes failed to produce crystals, which was perhaps a result of more than 100-fold weaker binding to MINTS (Nicoll *et al.*, 2006), the complex with Pd^{II} formed crystals that diffracted to a similar resolution (1.1 Å) as the Cu^{II}-bound form, albeit with different space-group symmetry. The MINTS peptide contains the structural diversity of a protein (an α-helix, loop regions, disulfide bridges and a metal-binding site), justifying its characterization as a miniprotein. Presumably owing to its compact size, well diffracting crystals of metal-bound MINTS could be obtained from a standard sparse-matrix reagent screen without further optimization.

The presence of disulfide bonds and of a heavy-metal centre in conjunction with high-resolution diffraction offered the opportunity to test alternative phasing approaches based on data recorded from a single crystal using either single-wavelength anomalous dispersion (SAD) or the recently introduced method of radiation-damage-induced phasing (RIP; Nanao *et al.*, 2005; Ravelli *et al.*, 2003; Zwart *et al.*, 2004). Primary radiation damage has re-emerged as a significant problem on the high-flux beamlines of third-generation synchrotron sources. While the propagation of reactive radicals is dramatically reduced in cryocooled (~100 K) specimens (Ravelli & McSweeney, 2000), protein or DNA crystals nonetheless incur primary damage. Being dependent on the accumulated dose but largely independent of sample temperature, primary radiation damage can render phasing by multi-wavelength anomalous dispersion (MAD) or multiple isomorphous replacement (MIR) impossible (Ravelli & Garman, 2006). However, systematic analyses of X-ray diffraction data sets from frozen crystals recorded over prolonged periods of time revealed characteristic 'fingerprints' of radiation damage, such as increased atomic *B* factors and unit-cell volumes, small rotations/translations of molecules in the unit cell, breakage of disulfide bonds or decarboxylation of acidic residues (Ravelli & McSweeney, 2000; Burmeister, 2000; Borek *et al.*, 2007). Specific radiation-induced structural changes, such as broken bonds and concomitant shifts of electron-rich atoms, can be exploited to obtain experimental phase information (Ravelli *et al.*, 2003; Nanao *et al.*, 2005; Banumathi *et al.*, 2004; Zwart *et al.*, 2004; Ramagopal *et al.*, 2005). This is typically performed by recording a sequence of low-dose data sets of the same crystal, interspersed with exposure of the (frozen) crystal to the unattenuated beam. The substructure of radiation-sensitive sites (*e.g.* disulfide bridges or metal sites) is determined by comparing the 'before' data set with the 'after' data set in a procedure resembling phasing by MIR, where the 'after' data set assumes the role of the native crystal (Nanao *et al.*, 2005).

Here, we report the crystal structure of the Pd^{II}-bound form of the MINTS peptide and analyse the outcomes of crystallographic phasing by SAD and RIP for the Cu^{II}-bound and Pd^{II}-bound forms of MINTS. Despite identical amino-acid sequences of the peptide component, we observed differential specific radiation damage as the basis for RIP phasing in the two metal-bound complexes of MINTS.

2. Materials and methods

2.1. Peptide synthesis and crystallization

The synthesis of MINTS and the crystallization of Cu-bound MINTS have been described previously (Nicoll *et al.*, 2006). Diffraction-quality crystals of Pd^{II}-bound MINTS

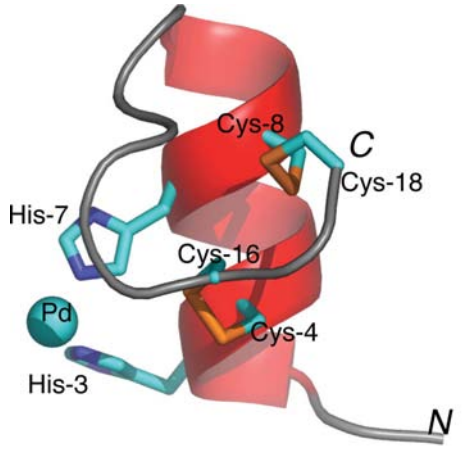

Figure 1
Ribbon representation of Pd^{II}-bound MINTS. The side chains of His-3 and His-7 and of the cysteine residues are shown as sticks. The sequence of MINTS and that of the related NTH-18 peptide (Nicoll *et al.*, 2005) are shown below, with amino-acid substitutions boxed.

Table 1
Reflection data statistics.

Values in parentheses are for the high-resolution shell.

	Cu-MINTS		Pd-MINTS		
	Before	After	Mpd7-Before†	Mpd7-After2	Mpd3
Station‡	ID14-4	ID14-4	ID14-4	ID14-4	In-house
Wavelength (Å)	0.97857	0.97857	0.93926	0.93926	1.5418
Space group	$P6_322$		$P4_12_12$		$P4_12_12$
Unit-cell parameters (Å)					
$a = b$	44.35	44.40	30.45	30.49	30.40
c	58.36	58.48	48.12	48.15	48.17
Resolution limits	38.4–1.10 (1.16–1.10)	38.5–1.20 (1.27–1.20)	48.1–1.10 (1.16–1.10)	48.2–1.10 (1.16–1.10)	19.6–1.91 (2.01–1.91)
$R_{\rm merge}$§ (%)	10.3 (36.4)	9.8 (60.3)	5.4 (23.4)	6.1 (43.7)	4.4 (7.7)
No. of observations	471044 (65124)	119843 (13483)	71236 (10066)	71443 (10113)	11850 (1221)
Unique reflections	14358 (2027)	11186 (1560)	9757 (1387)	9769 (1381)	1990 (270)
Mean $I/\sigma(I)$	28.1 (10.2)	14.4 (3.2)	21.4 (7.3)	18.4 (4.1)	30.3 (18.5)
Completeness (%)	99.8 (99.2)	99.7 (98.1)	99.9 (99.8)	100 (99.9)	99.5 (97.7)
Multiplicity	32.8 (32.1)	10.7 (8.6)	7.3 (7.3)	7.3 (7.3)	6 (4.5)
Anomalous completeness (%)	99.7 (99.2)	99.7 (97.8)	99.9 (99.2)	100 (99.8)	98.4 (89.8)
Anomalous multiplicity	17.9 (17.1)	5.8 (4.6)	4 (3.9)	4 (3.9)	3.6 (2.7)
R(isom)¶ (%)		20.8		14.5	
$\langle\Delta F\rangle/\langle\sigma(\Delta F)\rangle$¶		2.39		2.52	

† The statistics for data sets Mpd7-Middle and Mpd7-After1 are reported in Supplementary Table 1. ‡ Beamline ID14-4 is at the ESRF, Grenoble, France. The in-house X-ray source was a MicroMax 007 HF generator with VariMax confocal optics (Rigaku, The Woodlands, Texas, USA). § $R_{\rm merge} = \sum_{hkl}\sum_i |I_i(hkl) - \overline{I(hkl)}|/\sum_{hkl}\sum_i I_i(hkl)$, where $I_i(hkl)$ is the intensity of the ith measurement of reflection hkl and $\overline{I(hkl)}$ is the mean value of $I_i(hkl)$ for all i measurements. ¶ Determined during data preparation in *SHELXC*.

were obtained from a sparse-matrix screen (Structure Screens 1 and 2; Molecular Dimensions Ltd). Prior to setting up the crystallization trials, the peptide solution (5 m*M*) was saturated with palladium acetate, centrifuged at 14 000 rev min^{-1} and decanted. Crystals of Pd^{II}-bound MINTS appeared about 2 d after mixing 1 µl protein solution with 1 µl reservoir solution over a reservoir of 0.2 *M* trisodium citrate, 0.1 *M* Na HEPES pH 7.5 and 30%(*v*/*v*) 2-methyl-2,4-pentanediol (MPD). Crystals were mounted in nylon loops and frozen in liquid nitrogen from the initial screen without further treatment.

2.2. X-ray data acquisition and structure determination

Diffraction data for RIP phasing of metal-bound complexes of MINTS were recorded on beamline ID14-4 at the European Synchrotron Radiation Facility (ESRF), Grenoble, France (Table 1, Supplementary Table 1[1]) in February 2005 and October 2006. Additional data were recorded for Pd-MINTS on beamline ID29 (Supplementary Table 1[1]) and on a microfocus rotating-anode generator with a copper target (Rigaku; Table 1). The data-recording protocols for the RIP data sets were as follows.

Cu-MINTS (ID14-4, February 2005): 'Before', 180 frames, 1 s per exposure (5% transmission), φ from −110° to +70° in 1° intervals and 180 frames, φ from +70 to +250° in 1° intervals; 'Burn', 30 s at full intensity; 'After', 400 frames, φ from +70° to 170° in 0.25° intervals, 1 s per frame (5% transmission).

Pd-MINTS (ID14-4, October 2006, crystal Mpd7): 'Before', 'Middle', 'After1' and 'After2' data sets were recorded with the following parameters: 200 frames, φ from +30° to +130° in 0.5° intervals, 1 s per frame at 10% transmission, with exposure to the unattenuated beam for 30 s between data sets. The RIP signal was sufficient for phasing between the 'Before' and 'After2' data sets.

Reflection statistics in Table 1 (and Supplementary Table 1[1]) were obtained from an analysis run in *SCALA* (Evans, 1997) of data integrated and scaled in *XDS*/*XSCALE* (Kabsch, 1993) without applying the 'zero-dose correction'. RIP phasing was carried out using *SHELXC*/*D*/*E* (Sheldrick, 2008). Reflection files for RIP phasing were generated using *SHELXC* as described in Nanao *et al.* (2005). The substructure was determined using *SHELXD* (Sheldrick, 2008) and the phases were solvent-flattened in *SHELXE* (Sheldrick, 2008; Supplementary Table 2[1]). In SAD phasing, heavy-atom sites were determined using *SHELXD* within the *autoSHARP* interface (Vonrhein *et al.*, 2006). Positions were refined and phases were calculated using *SHARP* (de La Fortelle & Bricogne, 1997) and the phases were solvent-flattened using *SOLOMON* (Abrahams & Leslie, 1996). Models of the MINTS peptide were built manually in *Coot* (Emsley & Cowtan, 2004) and refined using *REFMAC*5 (Murshudov *et al.*, 1997). Thermal displacement parameters were modelled initially by individual isotropic *B* factors. In the final stages of the refinement, individual anisotropic temperature factors were refined. The final model comprises residues 1–18 of the MINTS peptide, one palladium ion and two ordered molecules of the precipitant MPD. Refinement statistics for the model of Pd^{II}-bound MINTS are listed in Table 2.

2.3. Analysis of phasing

Phase-error and map-correlation analysis was carried out using the *CLIPPER* utility *PHASEMATCH* (Kevin Cowtan; http://www.ysbl.york.ac.uk/~cowtan/clipper/clipper.html) and

[1] Supplementary material has been deposited in the IUCr electronic archive (Reference: HV5095). Services for accessing this material are described at the back of the journal.

Table 2
Statistics of structure refinement of Pd^{II}-bound MINTS with geometry restraints.

Resolution (Å)	48–1.10
R_{cryst}/R_{free}† (%)	15.2/15.5
No. of non-H atoms	
Total	169
Peptide	142
Metal	1
Water	10
MPD	16
Average *B* factors (Å^2)	
Overall	8.8
Peptide	7.36
Solvent	13.3
Wilson *B* factor (Å^2)	5.04
R.m.s.d. bonds (Å)	0.005
R.m.s.d. angles (°)	1.12
R.m.s.d. *B* of bonded atoms (Å^2)	
Main chain	0.5
Side chain	0.9
Ramachandran plot‡	
Most favoured (%)	80
Allowed (%)	20

† $R_{cryst} = \sum_{hkl} \big||F_o| - |F_c|\big| / \sum |F_o|$, where F_o is the observed structure-factor amplitude and F_c is the calculated structure-factor amplitude. R_{free} is the same but was calculated based on 5% of reflections not used in the refinement. ‡ The Ramachandran plot statistics were determined using *PROCHECK* (Collaborative Computational Project, Number 4, 1994).

OVERLAPMAP (Collaborative Computational Project, Number 4, 1994). Experimental phases were compared with σ_A-weighted model phases derived from the refined coordinate set.

3. Results

3.1. Structure of the Pd^{II}-bound MINTS peptide

The Pd^{II}-bound and Cu^{II}-bound forms of the MINTS peptide gave rise to different crystal forms (Table 1): a hexagonal lattice with two peptides per crystallographic asymmetric unit (ASU) for Cu-MINTS and a tetragonal lattice with one peptide per ASU for Pd-MINTS. The structures were determined *de novo* using single-wavelength anomalous dispersion (SAD; Dauter *et al.*, 2002) or RIP phasing (Ravelli *et al.*, 2003; Supplementary Table 2), yielding high-quality experimental maps in either case (Fig. 2). Likewise, a readily interpretable map of Pd-MINTS was obtained based on SAD data to 1.9 Å recorded in-house from crystal Mpd3 (Supplementary Fig. S1*a*). The structure of Pd-MINTS was refined against the 'Mpd7-Before' data set (Tables 1 and 2) to 1.1 Å with geometry restraints in place, initially describing thermal displacement by individual isotropic *B* factors. Subsequently, individual anisotropic *B* factors were refined and two molecules of 2-methyl-2,4-pentanediol (MPD) were included in the model, leading to a final free *R* factor of 15.5% (R_{cryst} = 15.2%) for the geometrically restrained model reported in Table 2. Release of the geometric restraints in five cycles of *REFMAC*5, with an observables-to-parameter ratio of 6.1, decreased the R_{cryst} and R_{free} values to 11.8% and 13.1%, respectively. As a result, the average deviations from ideal stereochemistry increased (r.m.s.d. bonds = 0.033 Å, r.m.s.d. angles = 2.8°), but all residues remained in the most favoured or allowed regions of the Ramachandran plot and we observed no material changes in the model or the calculated density.

The structure of Pd-MINTS comprises a two-turn N-terminal α-helix followed by a C-terminal loop of noncanonical secondary structure that is tethered to the helix through crossed disulfide bonds Cys-4–Cys-16 and Cys-8–Cys-18 (Fig. 1). The tether forces three near-90° bends onto the conformation of the C-terminal loop, with parts of the peptide backbone running parallel (residues 13–15, 17–18) or perpendicular (residue 15–17) to the helix axis. Irrespective of the covalent tether, the peptide backbone shows considerable conformational flexibility between Ala-10, the terminal residue of the helix, and Cys-16, the first of the disulfide anchors (Fig. 3). A moderate level of flexibility was already apparent when comparing the non-equivalent molecules in the previously reported crystal structure of Cu-MINTS (Nicoll *et al.*, 2006), but the differences are more pronounced between Cu^{II}-bound MINTS and Pd^{II}-bound MINTS owing to differing packing contacts: the C^{α} positions of Pro-13 and Ala-14 are shifted by 3.3 and 4.1 Å, respectively (magenta arrows in Fig. 3), when aligning the three structures with respect to helix residues 2–10. The overall root-mean-square displacement (r.m.s.d.) of C^{α} positions in the same alignment is ∼1.5 Å between Pd-MINTS and Cu-MINTS and ∼0.8 Å between the two Cu^{II}-bound structures. In contrast, the helix geometry appears rigid, with an r.m.s.d. of C^{α} positions of less than 0.3 Å in any pairing of the MINTS peptide backbones.

The N-terminus of the helix is well defined in chain *A* of Cu-MINTS and in Pd-MINTS, but is partially disordered in chain *B* of Cu-MINTS. In chain *A* of Cu-MINTS the carbonyl of the N-terminal acetyl group forms a hydrogen bond to the amide N atom of Cys-4 and the side chain of Asp-1 donates $O^{\delta 1}$ to the coordination polyhedron of an adjacent copper site. In chain *B* of Cu-MINTS, the N-terminal aspartate and acetyl are rotated approximately 180° about the $C-C^{\alpha}$ bond of Asp-1 (Fig. 3). The same N-terminal conformation is seen in Pd-MINTS, in which the side-chain carboxylate of Asp1 forms hydrogen bonds to the amide of Cys-4 and the acetyl is exposed to solvent and partially disordered.

3.2. Metal coordination

Prior to obtaining the crystal structure data, EPR experiments (hyperfine splitting constant = 166×10^{-4} cm^{-1} and $g_{\|}$ = 2.302 for the 1:1 complex) had suggested O and N ligands for the copper sites in Cu-MINTS (Nicoll *et al.*, 2006). Indeed, the crystal structure of Cu-MINTS revealed that the metal sites were coordinated by His-3, His-7 and carboxylate or water ligands in square-pyramidal geometry. As the copper sites were on general positions, *i.e.* they did not coincide with a rotation or screw axis, ligand coordination was not constrained by the overall crystallographic symmetry. In contrast, the palladium site in Pd-MINTS is situated on a crystallographic twofold rotation axis, with symmetry-related MINTS peptides coordinating the metal in a slightly distorted square-planar geometry (Fig. 4*a*). The binding distances between Pd and the

$N^{\varepsilon 2}$ atoms of His-3 and His-7 differ (1.98 *versus* 2.10 Å); the discrepancy is ∼4.5 times the estimated coordinate error (0.025 Å based on the $R_{\rm free}$ value), suggesting that the observed difference is significant. The difference in bonding distances correlates with differences in the features of the electron density around the metal position. At a contour level of 1.2σ, there is strong bridging density between the symmetry-related His-3 residues in the SAD-phased experimental electron-density map (Fig. 2*b*). In contrast, bridging density between His-7 and His-7′ (where the prime denotes the symmetry mate) only appears in the RIP-phased experimental map (Fig. 2*a*). The bridging density is absent in the SAD density map of Pd-MINTS crystal Mpd1 (Supplementary Table 1 and Supplementary Fig. S1*b*) extending to 1.3 Å or the SAD-phased map of crystal Mpd3 (Table 1 and Supplementary Fig. S1*a*). This could suggest that the bridging density arises from radiation damage. Indeed, when phases are calculated on the basis of the first 100 frames of the 'Mpd7-Before' data set, covering a wedge of 50° (99% completeness, 3.7-fold redundancy), the bridging density is not observed (Supplementary Fig. S1*c*).

In the superimposition of the peptide chains of Cu^{II}-bound and Pd^{II}-bound MINTS (Fig. 3), it is apparent that the position of the metal site is variable relative to the histidine side chains, with Pd separated from the Cu_A site (where the subscript denotes association with chain *A* of Cu-MINTS) by 3.6 and 3.2 Å between the two non-equivalent copper sites. Such flexible positioning of the metal site relative to the helix is accommodated by corresponding adjustments of the position of the side chain of His-7 facilitated by small changes in side-chain torsion angles and the backbone conformation.

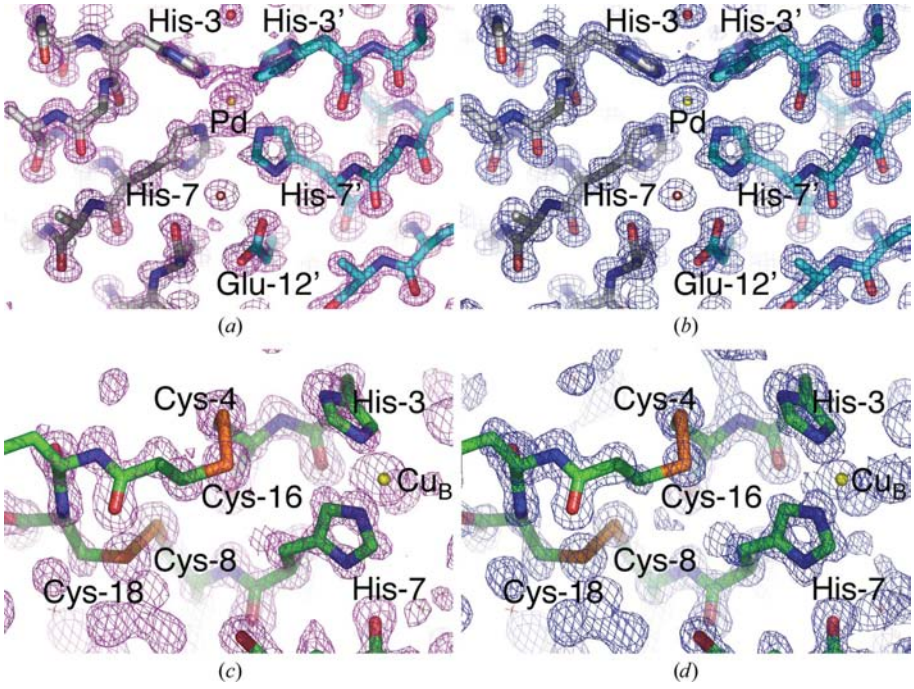

Figure 2
Experimental electron-density maps at 1.2 Å resolution contoured at 1.2σ of (*a*) Pd^{II}-bound MINTS phased by RIP, (*b*) Pd^{II}-bound MINTS phased by SAD, (*c*) Cu^{II}-bound MINTS phased by RIP and (*d*) Cu^{II}-bound MINTS phased by SAD. The final refined models are superimposed and selected amino acids are labelled.

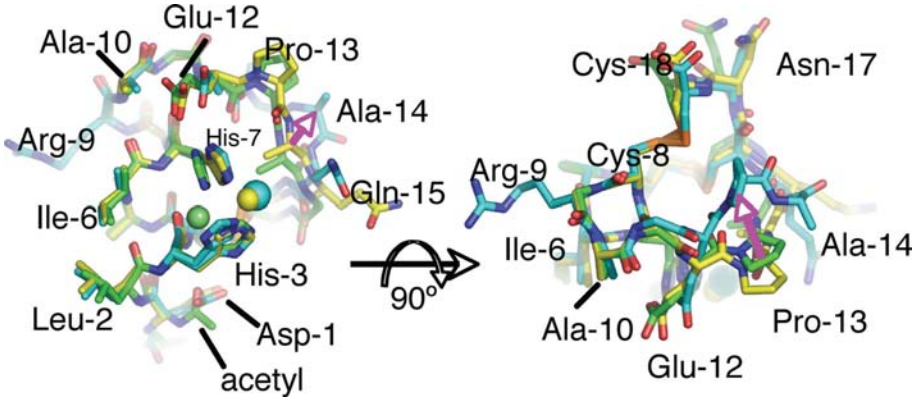

Figure 3
Two orthogonal views of the superimposition of the three crystallographically independent peptide chains of MINTS in complex with Cu^{II} (green and yellow) and with Pd^{II} (cyan). The views are related by a 90° rotation about the horizontal axis. Magenta arrows highlight the large positional shifts between the Pd^{II}-bound and Cu^{II}-bound structures.

3.3. RIP and SAD phasing

The structures of Cu-bound and Pd-bound MINTS were solved using phasing methods that exploit either the anomalous scattering of heavy atoms or the specific radiation damage incurred over recording repetitive data sets of the same crystal with intermittent 'burns' in the unattenuated beam. The chemical make-up of the MINTS peptide (a bound transition-metal ion in conjunction with two disulfide bonds) makes it a good candidate for an assessment of the RIP phasing method in comparison to SAD. While the peptide sequence is the same in both complexes, the Cu^{II}-bound and Pd^{II}-bound MINTS crystals belonged to different space groups and the question thus arose whether radiation damage would affect the two crystal forms in different ways.

Despite the data being recorded away from the respective absorption edges of copper (1.381 Å, *K* edge), palladium (3.44 Å, $L_{\rm I}$ edge) or sulfur (∼5 Å, *K* edge), the anomalous signal extended to 1.3 Å for Cu-MINTS and to 1.5 Å for the Pd-bound peptide (crystal Mpd7) as judged by $\langle D_{\rm ano}\rangle/\langle\sigma(D_{\rm ano})\rangle$ calculated in *SHELXC*. The heavy-metal sites (two Cu sites, one Pd site) were readily

determined using *SHELXD* (Sheldrick, 2008; Cu-MINTS, CC_{best} = 55.9, CC_{weak} = 31.8, PATFOM = 82.3; Pd-MINTS, CC_{best} = 36.9, CC_{weak} = 19.2, PATFOM = 22.5). Refinement of the heavy-atom sites in *SHARP* (de La Fortelle & Bricogne, 1997) and subsequent density modification in *SOLOMON* (Abrahams & Leslie, 1996) led to density maps of superb quality into which a model could be built manually without ambiguity.

Radiation-induced damage to the crystals is evident when comparing the unit-cell parameters (Table 1). The crystals of both Cu-MINTS and Pd-MINTS show a small but systematic increase in the unit-cell volume (Cu, +0.4%; Pd, +0.3%) over the course of data collection. The overall isomorphous difference calculated in *SHELXC* between the 'Before' and 'After' data sets was 20.8% for Cu-MINTS and 14.5% for Pd-MINTS (Table 1). Phasing the Pd-MINTS structure, the RIP signal $[\langle\Delta F\rangle/\langle\sigma(\Delta F)\rangle]$ between the 'Before' and 'After2' data sets was amplified by testing a range of scale factors to be applied to the 'After2' data in order to account for the overall loss of scattering power arising from radiation damage (see Nanao *et al.*, 2005). The best correlation coefficient (CC_{best}) in the *SHELXD* substructure search was obtained for a scale factor of 0.912, yielding the positions of the four Cys S atoms (Supplementary Table 2). This solution gave the correct hand and an interpretable map, although not the best pseudo-free correlation coefficient during density modification in *SHELXE*, which is usually a reliable indicator of a correct solution (Nanao *et al.*, 2005). In the RIP phasing of Cu-MINTS, the major heavy-atom sites found coincided with the copper positions (Supplementary Table 2), which is in striking contrast to Pd-MINTS, where the palladium site only appears as a low-occupancy site in the RIP substructure search (Supplementary Table 2). Conversely, only a single sulfur site

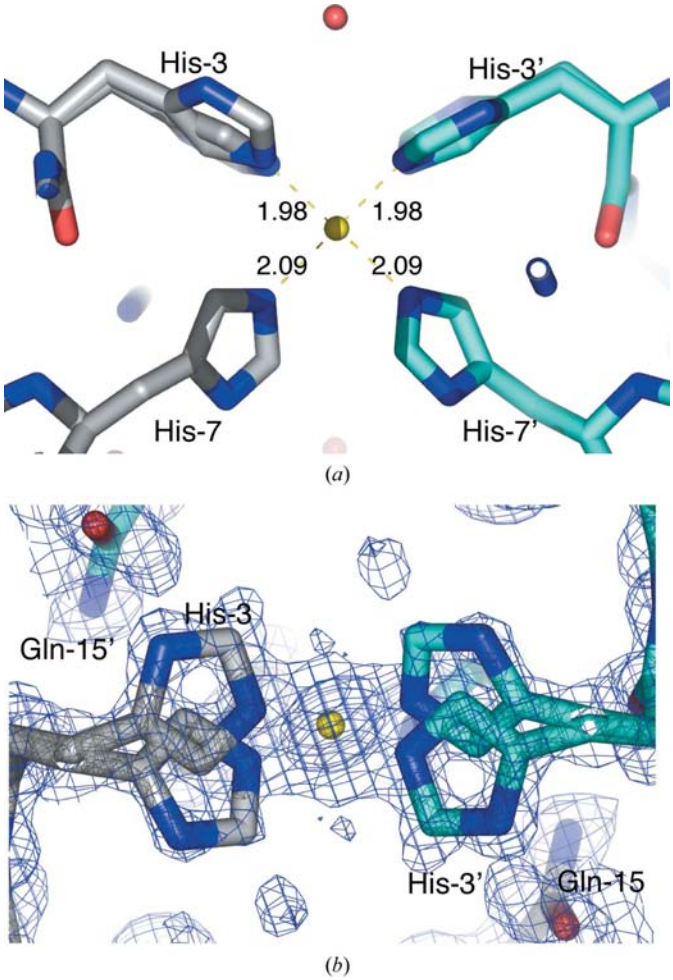

Figure 4
Coordination of the metal site in Pd-MINTS. (*a*) Pd—N bonding distances are indicated in angstroms. (*b*) SAD-phased experimental density at a 1.2σ contour level (1.2 Å resolution), indicating the dual conformation of His-3.

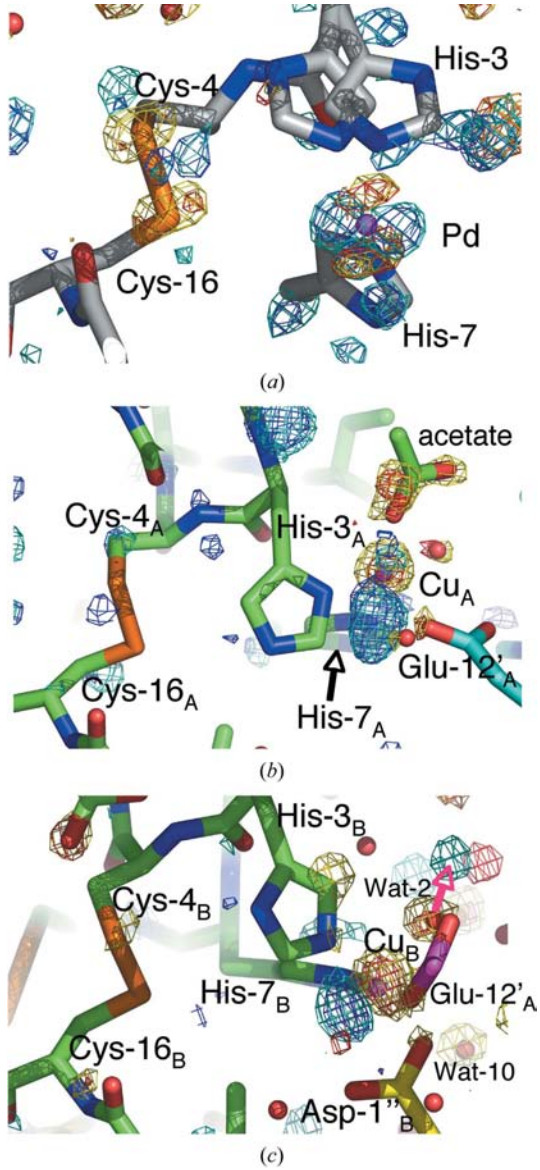

Figure 5
Difference Fourier density ($mF_o - DF_c$) around radiation-sensitive sites contoured at +3σ (blue, cyan) and −3σ (red, yellow) calculated on the basis of the refined model. Maps were calculated using the amplitudes of the 'Before' (blue and red) and 'After' (yellow and cyan) data. Residues are labelled with subscripts indicating the chain ID in (*b*) and (*c*) and primes denoting symmetry-related chains. (*a*) Pd-MINTS. (*b*) Cu-MINTS around site Cu_A. (*c*) Cu-MINTS around site Cu_B.

was detected in the RIP substructure search of Cu-MINTS (Supplementary Table 2). Interestingly, the minor sites found in RIP phasing of Pd-MINTS also include the carboxylate $O^{\delta1}$ of residue Asp-1 and a hydroxyl of one of the ordered MPD molecules. Carboxylate groups are often affected by specific radiation damage (Ravelli & McSweeney, 2000).

The sites found in the RIP-dependent substructure search correlate with the analysis of $F_o - F_c$ difference Fourier maps calculated with phases derived from the final models. In Pd-MINTS, strong negative difference density (indicating a loss of electron density) is apparent at the Cys-4–Cys-16 disulfide bond when calculating the Fourier synthesis with coefficients $F_{o,After2} - F_c$, where $F_{o,After2}$ are the observed structure-factor amplitudes of the 'After2' data set (Table 1, Fig. 5*a*). The negative density increases markedly from the 'Before' to the 'After2' data, while a positive density peak appears next to the negative peak, suggesting breakage of the Cys-4–Cys-16 disulfide bond. A similar but less pronounced change in the difference density is apparent for the Cys-8–Cys-18 disulfide bond (Supplementary Figure S2*a*), whereas in Cu-MINTS the disulfide bonds show no or comparatively only weak difference density peaks at the disulfide bonds (Supplementary Figs. S2*b* and S2*c*). The palladium site, which is surrounded by both positive and negative difference density, shows no change in this density as a function of exposure time (Fig. 5*a*). In the difference Fourier density map the copper sites appear smeared out, with a distinct increase in negative density for both sites (Figs. 5*b* and 5*c*).

The experimental density maps in all four phasing scenarios were of excellent quality (Fig. 2) and completely defined the peptide structure (except for the disordered side chain of Arg-9 in Cu-MINTS). The SAD map for Pd-MINTS clearly indicated a dual conformation for His-3 (Fig. 4*b*), which was also apparent in $F_o - F_c$ difference Fourier maps calculated on the basis of a single conformer model (Supplementary Fig. S3). The phase errors of the (density-modified) experimental phases were calculated using *PHASEMATCH* (see §2) against the FOM-weighted model phases of the final refined model. Truncating the reflection files at 1.2 Å, the overall weighted mean phase errors (wMPE) were 19.6° and 31.2° for the Pd-MINTS RIP and SAD phases, respectively, and 15.4° and 28.6° for the Cu-MINTS RIP and SAD phases, respectively (Supplementary Table 2). These overall values suggest that the RIP phases were superior. Plotting the wMPE *versus* resolution (Fig. 6), it is interesting to note that the phase error of the RIP phases is more or less flat, while that of the SAD phases increases steadily towards higher resolution. In contrast, the map correlation coefficients do not display a pronounced difference (Supplementary Table 2). This is consistent with the visual impression of the electron-density maps, which do not convey a marked difference in quality.

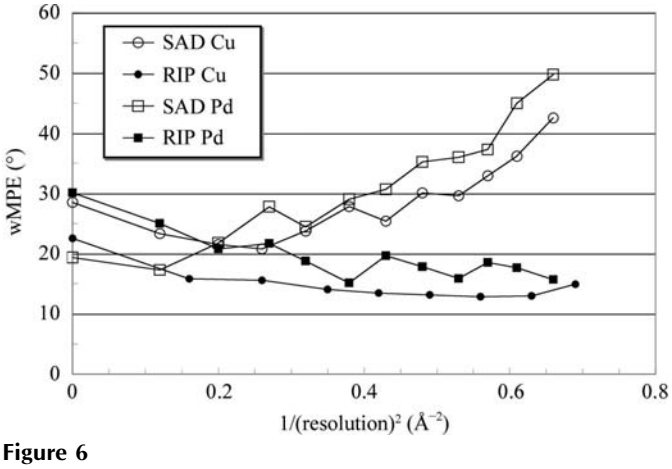

Figure 6
Weighted mean phase error (wMPE) of experimental phases relative to model phases of the final refined model.

4. Discussion

The structure of Pd^{II}-bound MINTS reported here reinforces the view that the binding of transition metals promotes a regular α-helical geometry of MINTS over the N-terminal ten residues of the peptide. While the precise location of the metal site with respect to the peptide structure may vary within boundaries determined by the stereochemical properties of His-3 and His-7, this has no noticeable effect on the helix geometry, as is apparent from the superimposition of the Cu^{II}-bound and Pd^{II}-bound peptides. The apparent 'stiffness' of the α-helix is likely to be exaggerated owing to the densely packed three-dimensional lattice and averaging across the lattice in the diffraction experiment. However, the two structures differ markedly C-terminal to the helix (Fig. 3) despite the steric constraints imposed by the disulfide tethers. Significant structural flexibility in the N-terminal helix was observed in the ensemble of two-dimensional NOESY- and TOCSY-based structures of the closely related NTH-18 peptide (Nicoll *et al.*, 2005). It does not seem too far-fetched to anticipate similar flexibility in the helix of MINTS in the solution state when either copper or palladium is bound. NMR-based structural analysis of these complexes is hampered by the paramagnetic properties of the metals and the requirement for low-pH conditions, under which the His residues are protonated. An attempt at obtaining ^{1}H NMR spectra for structure determination of the metal-free form indicated that MINTS was significantly more disordered than NTH-18, in line with the CD results, hinting at a largely 'dissolved' N-terminal helix (Günther, Nicoll and Allemann, unpublished data).

Comparing the crystal lattices of Cu^{II}-bound and Pd^{II}-bound MINTS, it is striking that the molecular packing in the hexagonal lattice of Cu-MINTS is dominated by direct peptide–peptide contacts, as the two largest interfaces in terms of buried solvent-accessible surface do not involve a metal ion. While metal-mediated inter-peptide contacts are present, these play a lesser role. In Pd-MINTS, the palladium site is the centre point of two intertwined peptides (Fig. 7): in addition to the Pd-mediated contacts between symmetry-related histidine residues, this interface includes inter-peptide polar contacts, duplicated by symmetry, between the side chain of Glu-12 and the amide N atom of Ala-14, and between Gln-15 and the carbonyl O atom of His-3, as well as significant hydrophobic contacts between the aliphatic C atoms of the symmetry-

related Glu-12 side chains. While the notion of a Pd^{II}-mediated MINTS dimer remains untested in solution, the crystal lattice of Pd-MINTS (Supplementary Fig. S4) appears to be built from the quasi-dimeric units shown in Fig. 7.

Local environment is an important factor in determining the susceptibility to radiation damage of a given group (Ravelli & McSweeney, 2000); hence, differences in crystal packing may explain the differential radiation damage observed in the Pd^{II}-bound and Cu^{II}-bound versions of the MINTS peptide. The present crystal structures revealed several of the hallmarks of radiation damage, including an increase in unit-cell volume, shift of metal sites, reduction of disulfide bonds and (partial) decarboxylation. RIP phasing of Cu-MINTS rested on the two copper sites, with little or no contribution from the disulfide bridges. However, RIP phasing of Pd-MINTS rested primarily on the disulfide bonds, with only a minor signal from the palladium site (Supplementary Table 2). This is surprising given that metal centres suffer radiation-induced reduction and are counted amongst the sites that are most sensitive to primary radiation damage (Ravelli & McSweeney, 2000). While there are subtle changes in the difference density features around the palladium site between the 'Before' and 'After2' data sets, these changes are much weaker than those around the Cys-4–Cys-16 disulfide bridge, the site of the most pronounced changes in difference density as a function of radiation dose in Pd-MINTS. It is noteworthy that the Cys-4–Cys-16 disulfide bridge is spatially close to metal sites (5–7.5 Å), whereas the Cys-8–Cys-18 bond is shielded from the metal sites by other peptide atoms. In the superposition of the individual peptide chains with their respective metal site, it is apparent that the Cu_B site after the burn is closer to that of palladium in Pd-MINTS, which implies a shift towards the Cys-4–Cys-16 bond. A more dramatic shift can be seen for the Cu_A site, yet this site is positioned differently with respect to the His residues, which effectively shield the metal site from the Cys-4–Cys-16 disulfide bond. Given the close proximity of the metal site, in particular for Cu_B and Pd, electron transfer from the metal site to the Cys-4–Cys-16 seems conceivable and might play a role in how radiation affects the structure.

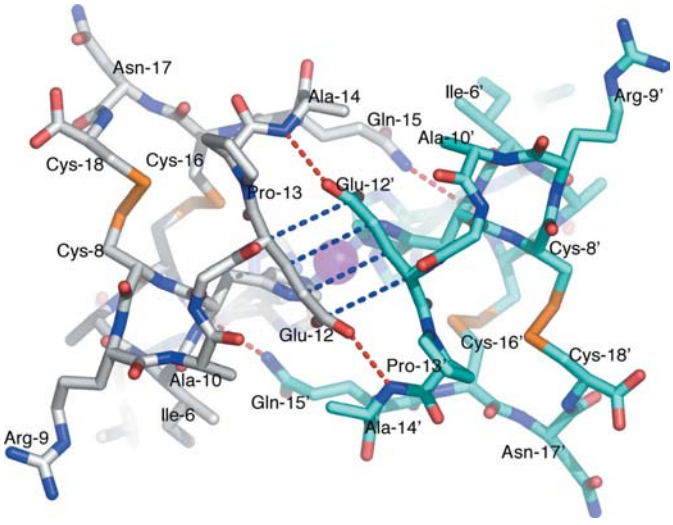

Figure 7
Pseudo-dimer of Pd-MINTS mediated by the palladium site, which is located on a twofold rotation axis. Selected interactions between the peptide chains are indicated in red (hydrogen bonds) and blue (hydrophobic interactions).

A second factor that might explain the differential effects of ionizing radiation on the respective structures is the constraint imposed on the metal sites by crystallographic and local symmetry. Firstly, the coordination of the Pd site is highly symmetric by virtue of the fact that this site is located on a crystallographic symmetry axis. Secondly, the ligands of the palladium site are four peptide side chains from two symmetry-related peptides, whereas the copper sites are coordinated by a mix of peptide side chains from two or more symmetry-related chains plus ordered solvent groups (Figs. 5*b* and 5*c*; Nicoll *et al.*, 2006). For instance, the difference density around the Cu_A site indicates that the acetate molecule disappears as the metal ion shifts away from its initial position. Similarly, the water molecule (Wat-2) forming the tip of the square pyramid of the Cu_B coordination polyhedron shifts ~1.6 Å away from the initial site as the copper ion shifts in the opposite direction (Fig. 5*c*).

While the experimentally derived electron-density maps, irrespective of phasing method, appear to be of very similar quality judged by visual impression or overall map correlation coefficient, the resolution-dependence of the weighted mean phase errors are distinctly different between the two approaches and can perhaps be attributed to the different software packages used for phase calculation and density modification.

5. Conclusion

The present analysis shows that changes in crystal packing and local symmetry of metal sites influences the susceptibility of peptide structures of identical amino-acid composition to ionizing radiation. Electron transfer between spatially close radiation-sensitive groups might be a factor that could possibly explain differential radiation damage. The crystal structures of MINTS in complex with either Pd^{II} or Cu^{II} suggest a well defined helical geometry, but comparison with the NMR-derived structure of the closely related but non-metal-binding NTH-18 peptide cautions that constraining the peptide on a tightly packed crystal lattice may exaggerate the apparent stability of the metal-binding-induced helix formation. Its compact size, ease of crystallization and versatile metal-binding properties in conjunction with disulfide-bond structure suggest that MINTS could be used as a test specimen for method development in crystallographic phasing as well as beamline testing. Furthermore, with its metal-binding properties, the MINTS sequence might be suitable as a 'phasing tag' for larger proteins: attached to either terminus, the MINTS peptide could provide an engineered heavy-atom-binding site, allowing phasing of the larger polypeptide. In this context, we note the recent MAD phasing of a 30 kDa protein based on Ni^{2+}-induced ordering of the N-terminal histidine-affinity tag (Ghadbane *et al.*, 2007).

We thank ESRF Grenoble for access to beamlines and travel support and the ESRF staff for assistance during data collection. AJN was supported by a PhD studentship from the UK Engineering and Physical Sciences Research Council (EPSRC).

References

Abrahams, J. P. (1997). *Acta Cryst.* D**53**, 371–376.

Abrahams, J. P. & Leslie, A. G. W. (1996). *Acta Cryst.* D**52**, 30–42.

Banumathi, S., Zwart, P. H., Ramagopal, U. A., Dauter, M. & Dauter, Z. (2004). *Acta Cryst.* D**60**, 1085–1093.

Borek, D., Ginell, S. L., Cymborowski, M., Minor, W. & Otwinowski, Z. (2007). *J. Synchrotron Rad.* **14**, 24–33.

Burmeister, W. P. (2000). *Acta Cryst.* D**56**, 328–341.

Collaborative Computational Project, Number 4 (1994). *Acta Cryst.* D**50**, 760–763.

Dauter, Z., Dauter, M. & Dodson, E. J. (2002). *Acta Cryst.* D**58**, 494–506.

Emsley, P. & Cowtan, K. (2004). *Acta Cryst.* D**60**, 2126–2132.

Evans, P. R. (1997). *Proceedings of the CCP4 Study Weekend. Recent Advances In Phasing*, edited by K. S. Wilson, G. Davies, A. W. Ashton & S. Bailey, pp. 97–102. Warrington: Daresbury Laboratory.

Ghadbane, H., Brown, A. K., Kremer, L., Besra, G. S. & Fütterer, K. (2007). *Acta Cryst.* F**63**, 831–835.

Goodman, C. M., Choi, S., Shandler, S. & Degrado, W. F. (2007). *Nature Chem. Biol.* **3**, 252–262.

Guerrero, L., Smart, O. S., Weston, C. J., Burns, D. C., Woolley, G. A. & Allemann, R. K. (2005). *Angew. Chem. Int. Ed. Engl.* **44**, 7778–7782.

Guerrero, L., Smart, O. S., Woolley, G. A. & Allemann, R. K. (2005). *J. Am. Chem. Soc.* **127**, 15624–15629.

Johnsson, K., Allemann, R. K., Widmer, H. & Benner, S. A. (1993). *Nature (London)*, **365**, 530–532.

Kabsch, W. (1993). *J. Appl. Cryst.* **26**, 795–800.

La Fortelle, E. de & Bricogne, G. (1997). *Methods Enzymol.* **276**, 472–494.

Murshudov, G. N., Vagin, A. A. & Dodson, E. J. (1997). *Acta Cryst.* D**53**, 240–255.

Nanao, M. H., Sheldrick, G. M. & Ravelli, R. B. G. (2005). *Acta Cryst.* D**61**, 1227–1237.

Nicoll, A. J. & Allemann, R. K. (2004*a*). *Recent Res. Dev. Chem.* **2**, 227–243.

Nicoll, A. J. & Allemann, R. K. (2004*b*). *Org. Biomol. Chem.* **2**, 2175–2180.

Nicoll, A. J., Miller, D. J., Fütterer, K., Ravelli, R. & Allemann, R. K. (2006). *J. Am. Chem. Soc.* **128**, 9187–9193.

Nicoll, A. J., Weston, C. J., Cureton, C., Ludwig, C., Dancea, F., Spencer, N., Smart, O. S., Gunther, U. L. & Allemann, R. K. (2005). *Org. Biomol. Chem.* **3**, 4310–4315.

O'Neil, K. T. & DeGrado, W. F. (1990). *Science*, **250**, 646–651.

Ramagopal, U. A., Dauter, Z., Thirumuruhan, R., Fedorov, E. & Almo, S. C. (2005). *Acta Cryst.* D**61**, 1289–1298.

Ravelli, R. B. & Garman, E. F. (2006). *Curr. Opin. Struct. Biol.* **16**, 624–629.

Ravelli, R. B., Leiros, H. K., Pan, B., Caffrey, M. & McSweeney, S. (2003). *Structure*, **11**, 217–224.

Ravelli, R. B. & McSweeney, S. M. (2000). *Structure*, **8**, 315–328.

Sheldrick, G. M. (2008). *Acta Cryst.* A**64**, 112–122.

Taylor, S. E., Rutherford, T. J. & Allemann, R. K. (2001). *Bioorg. Med. Chem. Lett.* **11**, 2631–2635.

Taylor, S. E., Rutherford, T. J. & Allemann, R. K. (2002). *J. Chem. Soc. Perkin Trans. 2*, pp. 751–755.

Turner, E. C., Cureton, C. H., Weston, C. J., Smart, O. S. & Allemann, R. K. (2004). *Chem. Biol.* **11**, 69–77.

Vonrhein, C., Blanc, E., Roversi, P. & Bricogne, G. (2006). *Methods Mol. Biol.* **364**, 215–230.

Weston, C. J., Cureton, C. H., Calvert, M. J., Smart, O. S. & Allemann, R. K. (2004). *ChemBioChem*, **5**, 1075–1080.

Zwart, P. H., Banumathi, S., Dauter, M. & Dauter, Z. (2004). *Acta Cryst.* D**60**, 1958–1963.